

The capillary bed offers the largest hemodynamic resistance to the cortical blood supply

Ian Gopal Gould¹, Philbert Tsai², David Kleinfeld²
and Andreas Linninger¹

Abstract

The cortical angioarchitecture is a key factor in controlling cerebral blood flow and oxygen metabolism. Difficulties in imaging the complex microanatomy of the cortex have so far restricted insight about blood flow distribution in the microcirculation. A new methodology combining advanced microscopy data with large scale hemodynamic simulations enabled us to quantify the effect of the angioarchitecture on the cerebral microcirculation. High-resolution images of the mouse primary somatosensory cortex were input into with a comprehensive computational model of cerebral perfusion and oxygen supply ranging from the pial vessels to individual brain cells. Simulations of blood flow, hematocrit and oxygen tension show that the wide variation of hemodynamic states in the tortuous, randomly organized capillary bed is responsible for relatively uniform cortical tissue perfusion and oxygenation. Computational analysis of microcirculatory blood flow and pressure drops further indicates that the capillary bed, including capillaries adjacent to feeding arterioles ($d < 10 \mu\text{m}$), are the largest contributors to hydraulic resistance.

Keywords

Mathematical modelling, microcirculation, blood–brain barrier, cerebral hemodynamics, cerebral blood flow

Received 1 October 2015; Revised 15 June 2016; Accepted 30 July 2016

Introduction

Biochemical signaling between cerebral microcirculatory blood flow and the supply of oxygen to the brain is critical for normal brain function as well as disease states including ischemia,^{1–6} micro-infarcts,^{7–9} and functional hyperemia.^{10–12} The functional interaction of cerebral hemodynamics, angioarchitecture, and brain cell metabolism is known as the neurovascular unit (NVU). It has been hypothesized that control of the NVU depends on the orientation and arrangement of the microvessels.^{13,14} Moreover, non-Newtonian hemodynamic effects such as plasma skimming or the Fahraeus–Lindqvist effect may contribute to homogeneous oxygen supply in the cerebral cortex.^{15–17} Experimental inaccessibility and microdimensions of the cortical tissue have so far limited the ability to verify these hypotheses. In this work, we combine an almost complete inventory of brain cells and blood vessels obtained from sizable sections of the mouse cortex with a first principles computational model to better elucidate microcirculatory blood and oxygen perfusion patterns.

The functional relationship between microcirculation, tissue topology, and oxygen supply has been the object of experimental and computational studies for over 30 years.^{18–22} The supply of oxygen from the blood to the surrounding tissue has been quantified in empirical^{23,24} and theoretical^{25,26} studies, but have typically been limited to a single blood vessel. However, single vessel studies fail to describe network effects. Recent attempts to explore networks employ hierarchal tree-like structures to model small sections of the microcirculation.^{3,27–31} However, experimental evidence has been unable to identify a hierarchal order

¹Department of Bioengineering, University of Illinois at Chicago, Chicago, IL, USA

²Department of Physics, University of California at San Diego, San Diego, CA, USA

Corresponding author:

Andreas Linninger, University of Illinois at Chicago, 851 S. Morgan St., Chicago, IL 60607, USA.
Email: linninge@uic.edu

to blood pressure,³² hematocrit,³³ red blood cell velocity,³⁴ or oxygen saturation. Other studies employed random geometric space filling methods^{35,36}; unfortunately, these structures did not conform to the vessel topology seen in microscopy. However, topology significantly affects oxygen exchange.^{13,37} Another study³⁸ reconstructed a microcirculatory network from a thin section of the human cortex; yet in the resulting shallow computational domain, most microvessels are intersected by boundaries, thus failing to achieve three-dimensional network connectivity. This model is also subject to delicate boundary condition choices which weakened its predictive power. Another study³⁹ combined human image data with a modified constructive geometric optimization algorithm⁴⁰ to synthesize a physiologically realistic, randomized model of the NVU. The topology of artificially generated NVUs is statistically equivalent to the topology of real networks obtained by laser microscopy.²¹ However, that study concerns the human cortex but not the mouse.

This paper presents simulation results of blood supply and oxygen delivery in a large section of the mouse brain covering the pial network, penetrating vessels, the complete capillary bed, and almost all neuronal and glial brain cells. Two-photon microscopy imaging data of the murine somatosensory cortex⁴¹ were used to create a physiologically accurate multi-scale computational model of the cortical microcirculation. Simulations predicted realistic values for red blood cell velocity, hematocrit and oxygen tension in blood vessels, extracellular space (ECS) as well as intracellular compartments.

Materials and methods

The methods section describes data acquisition of the four somatosensory cortex specimens in the mouse. The mathematical background for modeling non-Newtonian hemodynamics, oxygen transport across the blood-brain barrier (BBB), and metabolism in the extravascular space is given.

Data acquisition

In four specimens, homologous sections of the somatosensory cortex were extracted and imaged with two photon microscopy.⁴¹⁻⁴⁴ Each section, with volumes $V_1 = 1.14$, $V_2 = 1.94$, $V_3 = 2.85$, and $V_4 = 2.71$ mm³, respectively, extends the full depth of the cortex down to the white matter, covering about 1–2% of the gray matter of the entire mouse brain.⁴⁵ Brain cell nuclei were labeled with a DNA stain and their locations vectorized⁴²; neuronal nuclei were further labeled with a pan-neuronal marker. Neuronal cell density ranged from 120,727–208,509 cells/mm³. Glial cell distribution was sparser with a range of 42,976–141,319 cells/mm³.

All blood vessels were labeled with a fluorescent gel under conditions that preserved lumen interior diameter. The spatial arrangement and connectivity of blood vessels, including all capillaries, were recorded. Every vessel in the four data sets was assigned one of five labels: (i) pial artery, (ii) penetrating arteriole, (iii) capillary, (iv) penetrating venule, or (v) pial vein. Pial arteries and penetrating arterioles were separated into different groups according to the diameter and location within the section. Vessel segments close to the cortical surface (within 100 μ m) with a diameter larger than 10 μ m were considered pial arteries. Vessels branching from surface arterioles were labeled descending arterioles. The tree-like descending arterioles were traced until the capillary bed was reached. The capillary bed was separated from the penetrating arterioles assessing the branching order from the arterioles as well as a 6 μ m diameter cutoff. Vessels that were within three branching orders of a large arteriole in the direction of blood flow were considered to be penetrating arterioles. No effort was made to differentiate pre-capillary arterioles from post-arteriole capillaries. This was not performed in the parent study⁴¹ and requires differential labeling of smooth muscle versus pericytes.^{46,47} For example, the molecular marker for smooth muscle actin, or proteoglycan *NG2*, would be needed to label both smooth muscle and *actin*, while the marker for intermediate filament *desmin* would be needed to label arteriolar smooth muscle⁴⁸ only. A similar segregation based on size and branching order was applied in reverse to label penetrating venules and surface pial veins; specifically, a capillary-penetrating venules cutoff for diameters less than 6 μ m and a penetrating venules-pial veins cutoff for diameters less than 12 μ m within a depth of 100 μ m below the pia.

Biphasic blood flow computations

Microcirculation was modeled as a biphasic suspension consisting of red blood cells (RBCs) and plasma flowing through a network of interconnected cylindrical segments.¹⁷ Non-Newtonian blood viscosity was calculated as a function of the local hematocrit and vessel diameter.^{16,49,50} More theoretical background for bulk blood flow computations is given in Supplemental Information, and all boundary conditions are described in Table 1. Hematocrit distribution is computed using a drift-flux model described previously.¹⁷ RBCs and plasma distributions were computed using a kinetic plasma skimming model (KPSM)¹⁷ to determine the discharge hematocrit, H_d , and the RBC velocity in each segment. In the mass conservation for RBCs in equation (1), the flux of RBCs through a vessel, Q_{RBC} , is equal to the product of the bulk blood flow, Q , and the discharge hematocrit. An uneven distribution of RBCs

Table 1. Summary of boundary conditions used in the micro-circulatory perfusion computations.

	Biphasic blood flow	
	Pressure ^{32,51,52}	Hematocrit
Arterial inlet	120 mmHg	0.35
Venous outlet	5 mmHg	Fully developed, $\nabla H = 0$
Oxygen		
	RBC ⁵³	Plasma
Pial arterial inlet	68.4 mmHg	68.4 mmHg ^a
Pial venous outlet	Fully developed, $\nabla C_{RBC} = 0$	Fully developed ^a , $\nabla C_p = 0$
Tissue surface		No Flux
Tissue GW Interface		Cyclic
Tissue boundaries		Cyclic

^aIn equilibrium with RBC oxygen tension according to the Hill equation.

in each bifurcation results from the velocity difference between RBCs and plasma, known as *plasma skimming*. Red blood cell mass conservation is written for a single bifurcation in equation (2). The difference in discharge hematocrit for two daughter branches, H_2 and H_3 , and the parent vessel, H_1 , was determined by solving for the *adjusted hematocrit*, H^* . The adjusted hematocrit depends on kinematic plasma skimming coefficients, θ_i , which are geometric functions of the cross-sectional area fraction of daughter to parent vessels, A_i/A_1 , and the drift parameter, $M = 5.25$, given in Table 2.

$$\nabla \cdot (QH_d) = \nabla \cdot Q_{RBC} = 0 \quad (1)$$

$$Q_1 H_1 - Q_2 H_2 - Q_3 H_3 = 0 \quad (2)$$

$$H_2 = H_1 - \Delta H = \theta_2 \cdot H^* \quad H_3 = \theta_3 \cdot H^*$$

$$\theta_2 = \left(\frac{A_2}{A_1}\right)^{\frac{1}{M}} \quad \theta_3 = \left(\frac{A_3}{A_1}\right)^{\frac{1}{M}}$$

Table 2. Cerebral oxygen transport parameters used in this work.

Parameter	Description	Value	Units	Reference
α_{pl}	Plasma oxygen solubility	2.82×10^{-5}	$\text{mL O}_2 \cdot \text{mL}^{-1} \text{mmHg}^{-1}$	Christoforides ⁵⁵
α_t	ECS oxygen solubility	2.80×10^{-5}	$\text{mL O}_2 \text{ mL}^{-1} \text{mmHg}^{-1}$	Liu ⁵⁴
β	Hemoglobin – O ₂ binding capacity	0.52	$\text{mL O}_2 \cdot (\text{mL RBC})^{-1}$	Goldman ³⁷
D_{ECS}	ECS oxygen diffusivity	1.8×10^3	$\mu\text{m}^2 \cdot \text{s}^{-1}$	Mintun ⁵⁶
k_f	Forward rate of hemoglobin-O ₂ dissociation	50.0	s^{-1}	This Work
M	Plasma skimming coefficient	5.25	–	Gould ¹⁷
n	Hemoglobin saturation Hill coefficient	2.7	–	Ellis ⁵⁷
P_{50}	Oxygen tension for 50% hemoglobin saturation	37	mmHg	Ellis ⁵⁷
k_m	Mitochondrial oxygen metabolism	3.5	s^{-1}	This Work
R_{CMRO}	Oxygen metabolic rate (zeroth order)	2.6	$\mu\text{mol} \cdot \text{g}^{-1} \cdot \text{min}^{-1}$	Cui ⁵⁸
k_{CMRO}	Oxygen metabolic rate (first order)	1.0	s^{-1}	This Work
S_g	Glia cell surface area	1780	μm^2	Rodríguez ⁵⁹
S_m	Mitochondria surface area	3.75	μm^2	Hoppler ⁶⁰
S_n	Neural cell surface area	23,430	μm^2	Howard ⁶¹
U	Oxygen mass transfer coefficient ^a	1.77×10^3	$\mu\text{m}^2 \cdot \text{s}^{-1}$	Popel ⁶²
w_b	Endothelial Wall Thickness ^b	1-5	μm	Linninger ³⁹
w_n	Neuronal membrane thickness	40	nm	Schmitt ⁶³
w_g	Glial membrane thickness	20	nm	Schmitt ⁶³
w_m	Mitochondrial membrane thickness	10	nm	Sjostrand ⁶⁴
V_m	Mitochondria volume	1.83	μm^3	Hoppler ⁶⁰
V_n	Neuronal cell volume	5694	μm^3	Howard ⁶¹
V_g	Glial cell volume	869	μm^3	Williams ⁶⁵

^aPial vessels were assigned a mass transfer coefficient of zero. ^bFormula for wall thickness: $w_b = \theta + \delta$; arteries ($\theta = 0.2$, $\delta = 0.4$), capillaries ($\theta = 0$, $\delta = 1$), and veins ($\theta = 0.021$, $\delta = 0.94$).

Blood pressure boundary conditions were assigned to all pial vessels entering and leaving the domain using the choices described in Table 1. A discharge hematocrit of 0.35 was set for each inlet on the pial surface. The model further assumed a fully developed hematocrit field at the outlet (no change of hematocrit across the last segment).

Oxygen convection in erythrocytes and plasma

Oxygen convection in the blood stream and transport into the tissue was solved using a previously presented dual-mesh technique.^{17,39} Oxygen bound to hemoglobin, C_{HbO_2} , travels at the velocity of the RBC phase, u_{RBC} , as in equation (3). Axial oxygen diffusion within the cylindrical vessel segment was neglected. Furthermore, non-linear oxygen–hemoglobin dissociation kinetics^{37,54,66,67} from the erythrocytes to plasma were implemented. The rate of oxygen desaturation from hemoglobin to plasma, $\dot{R}_{R \rightarrow P}$, in equation (3) was given by a first-order kinetic rate law, described in equations (13) to (15) of Supplemental Information, where additional details on the full binding kinetics are provided. It is important to note that the proposed oxygen dissociation kinetics obeys to the well-known Hill equation when reaching equilibrium.

$$-u_{RBC} \cdot \nabla C_{HbO_2} - \dot{R}_{R \rightarrow P} = 0 \quad (3)$$

Free plasma oxygen, C_{pIO_2} , was convected with plasma phase velocity, u_{pl} , given in equation (4). Oxygen transported from the capillary bed across the endothelial membrane of the BBB was driven by the concentration difference between free oxygen in the plasma and in the ECS, C_{ECSO_2} .

Oxygen extraction across the BBB from the blood to the extravascular space in equation (4) is a function of vessel surface area, S_b , oxygen permeability of the endothelial tissue, U , and endothelial wall thickness, w_b . Wall thickness was modeled as a linear function of the vessel lumen diameter, d , for arteries, capillaries, and veins as annotated in Table 2.

$$-u_{pl} \cdot \nabla C_{pIO_2} + \dot{R}_{R \rightarrow P} - S_b \frac{U}{w_b} (C_{pIO_2} - C_{ECSO_2}) = 0 \quad (4)$$

At the pial arterial inlets, the bound oxygen tension was set to $pO_2 = 68.4$ mmHg, listed in Table 1, as measured by two photon microscopy.⁵³ This value corresponds to RBC saturation of 83%. The concentration of free plasma oxygen was set under the assumption of equilibrium between the RBC and plasma phases according to the Hill equation. At pial outlets, both free and bound oxygen fields were assumed to be fully developed.

Tissue oxygen diffusion and metabolism

Tissue oxygen leaving the vasculature across the BBB enters the ECS. The ECS was discretized into a uniform Cartesian grid of a fixed edge length. Blood flow, pressure, and oxygen profiles were shown to be independent of the domain discretization. Results of a comprehensive mesh independence study can be found in Supplemental Information. Each cubic tissue element may contain multiple blood vessels; therefore, its oxygen supply stems from multiple segments, N_v , as given in the summation term of equation (5). Extravascular oxygen can diffuse through the tissue characterized by the diffusion coefficient, D_{ECSO_2} . The cortical surface was assumed to be impermeable to oxygen as shown in Table 1. At the sides of the cortical section, cyclic boundary conditions were enforced by connecting faces on opposing sides of the specimen to emulate an infinite domain. A cyclic boundary condition was applied at the gray-white matter interface as well, connecting the left half to the right half. Because the specimens are thick, the boundary choices had a mild effect in the interior of the domain.³⁹

It has been shown previously³⁹ that the dual-mesh technique used here produces the same results as the analytical Krogh cylinder for a single capillary. However, Krogh's model cannot predict oxygen transfer in micro-circulatory networks. Oxygen exchange in the cortex depends on two critical factors outside the scope of the Krogh model: (i) three-dimensional angioarchitecture as well as (ii) axial diffusion through the ECS.

Oxygen metabolism in the extravascular tissue was computed with two distinct versions described in the next section. The first assumed a first-order rate law of oxygen consumption. The second approach also predicted subcellular oxygen gradients.

First-order rate law for tissue oxygen consumption. The first approach assumed first-order reaction kinetics. Accordingly, oxygen metabolism was equal to the product of the extracellular oxygen concentration, C_{ECSO_2} , the volume of each tissue cell, V_{ECS} , and the first-order cerebral metabolic rate of oxygen consumption, k_{CMRO} , as in equation (5).

$$\sum_{i=1}^{N_v} S_{b,i} \frac{U_i}{w_{b,i}} (C_{pIO_2,i} - C_{ECSO_2}) + \nabla \cdot D_{ECSO_2} \nabla C_{ECSO_2} - V_{ECS} k_{CMRO} C_{ECSO_2} = 0 \quad (5)$$

Intracellular oxygen tension approach. The second, more detailed approach aimed at computing intracellular oxygen tension gradients between the ECS, the cell cytoplasm, and the mitochondria. This subcellular

metabolism is anisotropic because it incorporates the spatial distribution of neuronal and glial nuclei. Oxygen consumption in each tissue cell depended on the number of neurons, N_n , and glial cells, N_g . Oxygen transport into the interior of each neuron was driven by the concentration gradient between the ECS and the neuronal cytoplasm, C_{nO_2} , as described in equation (6). Transport across the neuronal cell membrane was limited by its surface area, S_n , and the membrane thickness, w_n . Oxygen supplied into each glial cell was likewise determined by the concentration gradient between the ECS and the glial cytoplasm, C_{gO_2} , and was regulated by the glial membrane surface area, S_g , and its thickness, w_g .

$$\begin{aligned} & \sum_{i=1}^{N_v} S_{b,i} \frac{U_i}{w_{b,i}} (C_{pIO_2,i} - C_{ECSO_2}) + \nabla \cdot D_{ECSO_2} \nabla C_{ECSO_2} \\ & - \sum_{j=1}^{N_n} S_n \frac{U}{w_n} (C_{ECSO_2} - C_{nO_2,j}) \\ & - \sum_{k=1}^{N_g} S_g \frac{U}{w_g} (C_{ECSO_2} - C_{gO_2,k}) = 0 \end{aligned} \quad (6)$$

Oxygen metabolism in neurons. The oxygen conservation balance for each neuron is given in equation (7). Oxygen reaching the cytoplasm was transported into its mitochondria, C_{mnO_2} , the actual site of oxygen metabolism. The flux from the cytoplasm into the mitochondria was governed by the mass transport coefficient, U , the mitochondrial surface area, S_m , and its membrane thickness, w_m . In this study, the inner and outer membranes of the mitochondria were assumed to form a single layer.

$$S_n \frac{U}{w_n} (C_{ECSO_2} - C_{nO_2}) - \sum_{i=1}^{M_n} S_m \frac{U}{w_m} (C_{nO_2} - C_{mnO_2,i}) = 0 \quad (7)$$

Since mitochondria could not be imaged directly, their spatial distribution within the neuronal cell body was set as follows. Each neuron was assigned an average number of mitochondria,^{68,69} $M_n = 839$, whose locations were spatially distributed according to a probability distribution function⁶⁹ along the efferent dendrites and axon fiber using the cell nuclei coordinate as reference, shown in Figure 6(b). Axons were assumed to be oriented perpendicular to the cortical surface. This process of random mitochondria distribution was repeated for every neuron. The spatial allocation of mitochondria enabled us to approximate anisotropic reaction rates as a function of the known position of nuclei.

Oxygen transported across the mitochondrial membrane was consumed by the electron transport chain. The reaction rate was assumed to be of first order with a rate constant k_m . In equation (8), C_{mnO_2} is the concentration of oxygen within neuronal mitochondria, V_m , is the mitochondrial volume. Oxygen tension in the ECS, cells, and mitochondria was converted from molar concentrations using Henry's solubility, α_t , given in Table 2.

$$S_m \frac{U}{w_m} (C_{nO_2} - C_{mnO_2}) - V_m k_m C_{mnO_2} = 0 \quad (8)$$

Oxygen metabolism in glial cells. Oxygen concentration in the glial cytoplasm, C_{mnO_2} , and mitochondria, C_{mgO_2} , was computed using a similar approach as described for neurons according to equations (9) and (10). The number of mitochondria, $M_g = 283$, for each glial cell was taken from fractional density data.⁷⁰⁻⁷² The spatial distribution of the glial mitochondria was assumed to lie within a sphere around the nucleus as shown in Figure 6(a). The total rate of metabolized oxygen in each tissue cube depended on the number of mitochondria, which in turn is a function of the anisotropic spatial distribution of neurons and glial cells.

$$S_g \frac{U}{w_g} (C_{ECSO_2} - C_{gO_2}) - \sum_{i=1}^{M_g} S_m \frac{U}{w_m} (C_{gO_2} - C_{mgO_2,i}) = 0 \quad (9)$$

$$S_m \frac{U}{w_m} (C_{gO_2} - C_{mgO_2}) - V_m k_m C_{mgO_2} = 0 \quad (10)$$

Results

First, the topology of the microcirculation in the four primary somatosensory cortical sections was statistically examined. Next, blood flow and oxygen transport predictions are presented. Finally, trajectories of blood pressures, hematocrit, and RBC oxygen saturation along paths from the arterial inlets to venous outlets were analyzed.

Morphological statistical analysis

The multi-scale dimensions of the four cortical sections are displayed in Figure 1(a-b). Blood vessels embedded in the cellular matrix are displayed at multiple length scales, from pial vessels at the cortical surface down to the capillary bed. Probability density functions (PDF) describing the distribution of vessel diameter, length, volume, and surface area, as well as vessel and neuronal density, are shown in Figure 2.

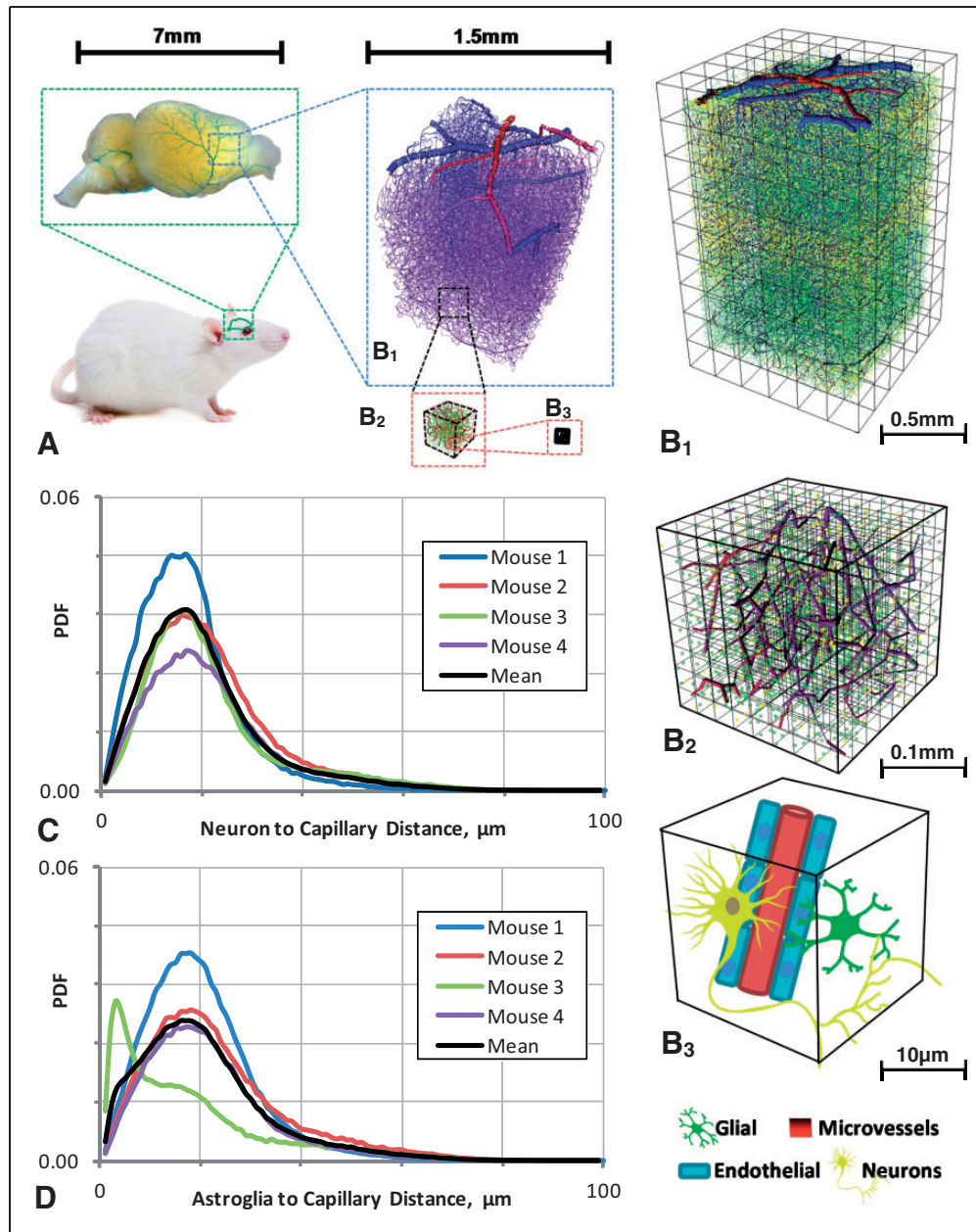


Figure 1. Vectorized data of the multi-scale vascular and cellular morphology of the mouse cerebral cortex. (a) Illustration of the multi-scale resolution of the murine cerebral vasculature from the cortical surface vessels down to the cellular level. (whole brain snapshot taken from the NIH supported KOMP Phenotyping Pilot project⁷³). (b) Full view of the microvascular network with cerebral arterioles in red, draining veins in blue, and capillaries in purple. Neuronal cells are displayed in yellow and glial cells in green at the 0.5 mm resolution. (Frames B₁ to B₃ show data in increasing magnification B₁. 1.0 mm × 1.0 mm × 1.2 mm, B₂. 200 µm × 200 µm × 200 µm, and B₃. 25 µm × 25 µm × 25 µm. At the finest resolution in B₃, cell bodies of neurons and glial cells were added for clarity). Histogram of cell to capillary distance for (c) neurons and (d) glial cells.

Distances of glial cells and neurons to the nearest capillaries were computed and reported as a PDF, shown in Figure 1(c) and (d). The mean distance between the neurons to the closest microvessel was 17.8 µm. The mean glial-capillary distance was 18.2 µm. The glial spacing in the third mouse specimen was shorter than the other three, as shown in Figure 1(d). For all metrics,

the variance within each data set was compared to the average of all four mouse cortical sections. Overall, the distribution of vessel length, diameter, and vessel density per volume was found to be statistically similar in all four data sets ($RSS < 0.04$). However, the surface area occupied by penetrating arterioles and venules was significantly smaller in the

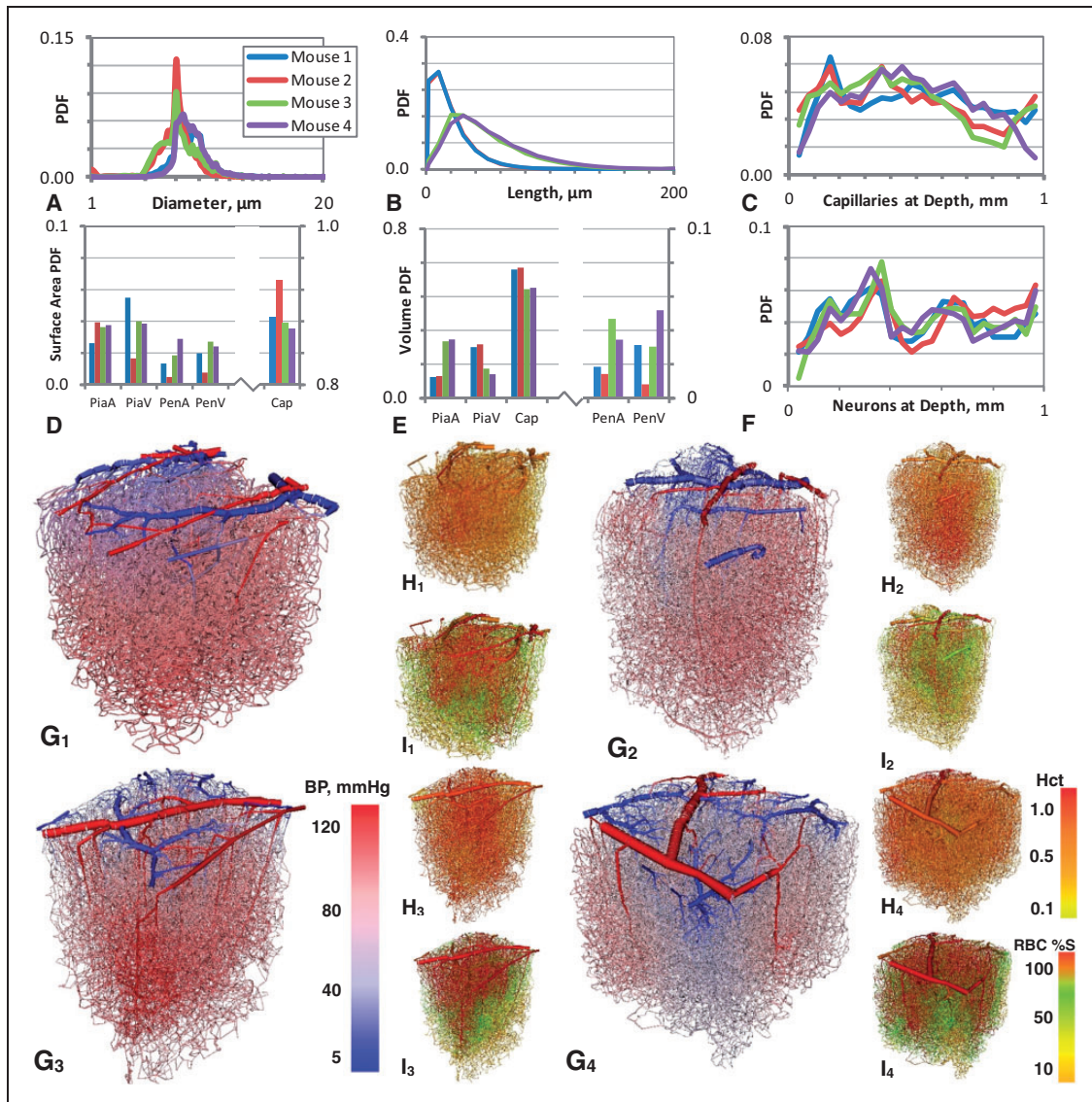


Figure 2. Statistical analysis of the four primary somatosensory cortical mouse data sets with superimposed hemodynamic simulation results. Probability density functions of anatomical parameters: (a) vessel diameter, (b) vessel length, and (c) the number of capillaries located at a given depth. Distributions for pial arteries (PiaA), pial veins (PiaV), penetrating arterioles (PenA), penetrating venules (PenV) and capillaries (Cap) with respect to (d) surface area, and (e) lumen volume fraction. (f) Probability density function of neuronal density at a given depth. (g-i) Computational results for blood pressure, hematocrit, and RBC saturation. Color-coding for (g) blood pressure from red (120 mmHg) to blue (5 mmHg), (h) hematocrit from orange (0.99) to green (0.11), and (i) RBC saturation from red (90%) to orange (10%).

second data set; see Supplemental Information for additional details.

A PDF for vessel diameters was constructed in Figure 2(a) showing an average diameter of $3.8 \pm 0.3 \mu\text{m}$. The diameter distribution of the capillary bed has a mean of $3.5 \pm 0.2 \mu\text{m}$. Vessel length distribution ranged from 1 to 200 μm as shown in Figure 2(b). The number of capillaries as a function of cortical depth is given in Figure 2(c). Capillary density was lowest near the cortical surface and at the gray-white matter interface at an approximate depth

of 0.8-0.9 mm. The volumetric ratio of blood vessels to tissue amounts to 0.8-1.5%, this result compares well to previous measurements.^{21,41,74} Vessel surface area is plotted in Figure 2(d) showing that the capillary bed occupies over 85% of surface area in all cortical samples. Figure 2(e) shows the distribution of volume fractions for each of the four data sets and Figure 2(f) plots the distribution of neurons as a function of depth.

The volume distributed as follows; pial arteries ($18.8 \pm 8.5\%$), penetrating arterioles ($2.9 \pm 1.3\%$),

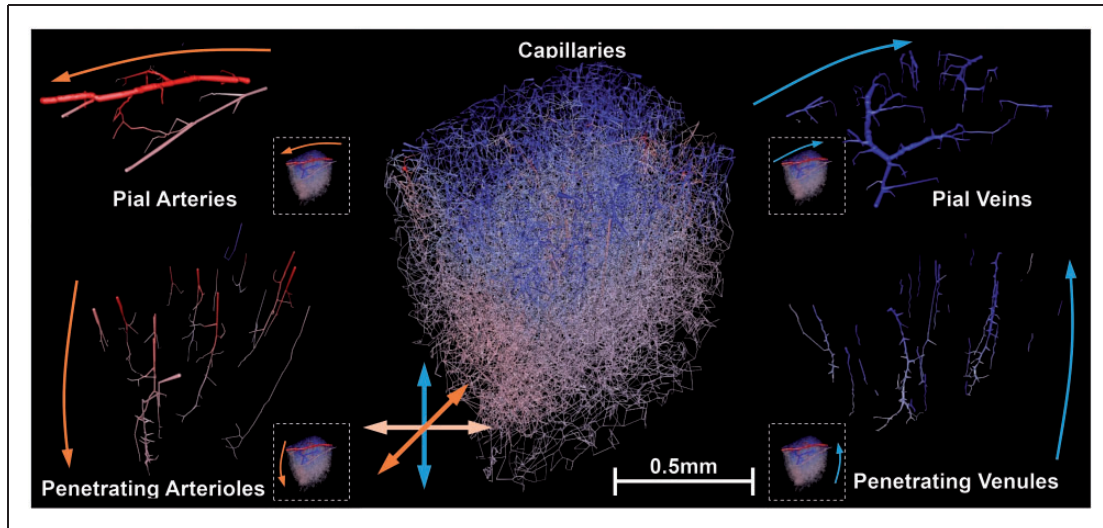


Figure 3. Depiction of the anatomical hierarchy of arterial, venous, and capillary microvessels in the primary somatosensory cortex for the first data set. Vessels are painted in colors corresponding to the blood pressure depicting arteries in red and veins in blue. Large surface pial vessels distribute blood along the surface of the cortex, and feed penetrating arterioles. Penetrating arterioles divert blood into deeper cortical layers. The capillary bed distributes blood uniformly in all directions. Venules collect the blood from the capillary bed and return it to the cortical surface. Pial veins convey the venous blood from the surface to the sinuses.

capillaries ($56.6 \pm 4.7\%$), penetrating venules ($3.1 \pm 1.5\%$), and pial veins ($18.7 \pm 6.2\%$). The total lumen of non-capillary vessels accounts for less than 45% of the entire microcirculatory blood volume. Data set 2 was an outlier in this distribution, with a sparse distribution of penetrating arterioles (1.4%) and penetrating venules (0.8%). Over 92% of all junctions in the capillary bed are bifurcations, only 7% are trifurcations, and 1% exhibit higher order connectivity.

Microcirculatory angioarchitecture. Figure 3 illustrates the anatomical hierarchy of the cortical angioarchitecture. The pial arteries form a network on the cortical surface. Long range pial arteries convey blood to more distal regions horizontally along the cortical surface. Penetrating arterioles siphon blood flow from the surface pials into the gray matter. These penetrating vessels carry blood perpendicular from the surface down to all six cortical layers. The distribution of microvessels in the capillary bed is isotropic with no apparent orientational preference. Finally, venules drain the capillary bed and penetrating venules bring blood back to the cortical surface where the pial veins discharge the blood into the venous sinuses.

Hemodynamics

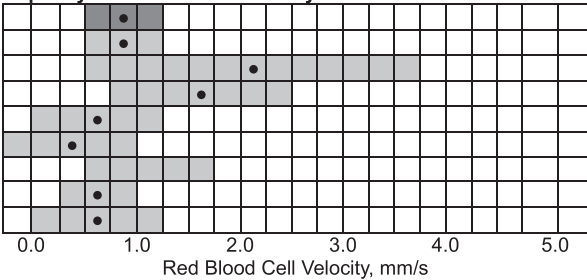
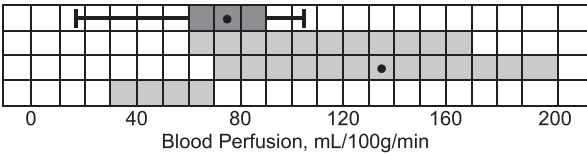
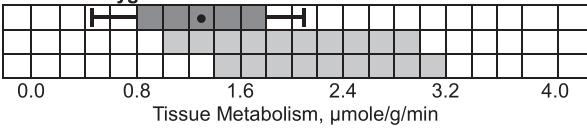
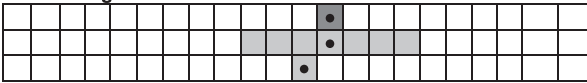
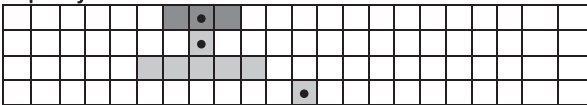
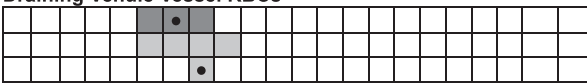
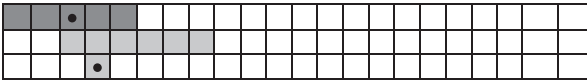
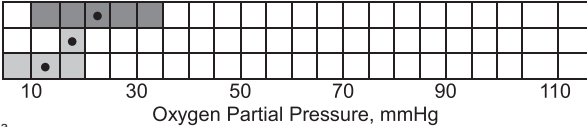
Figure 2(g-i) also depicts computed blood pressures, hematocrit, and RBC oxygen tension for all four mouse data sets. The main computational results are summarized in Table 3, which also shows comparisons to prior experimental studies. The distribution of RBC

velocities matches previous measurements⁷⁵ as can be seen in Figure 4(a). The average capillary RBC velocity was 0.93 ± 0.29 mm/s, which falls within the range of measurements shown in Table 3. RBCs in the penetrating arterioles travel at a speed of 14.18 ± 2.02 mm/s, and draining venules at 7.83 ± 1.11 mm/s. These speeds exceed RBC velocity in the capillary bed. Bulk blood velocity (RBCs and plasma together) through penetrating arterioles and veins was compared to recent ultrafast ultrasound localization microscopy measurements.⁷⁶ Reported blood velocity acquired by ultrasound in descending vessels ranged between 1 and 14 mm/s, comparable to computational predictions in both penetrating arteries, 9.51 ± 1.32 mm/s, and penetrating venules, 5.26 ± 0.74 mm/s. The discharge hematocrit in the capillary bed agrees with two-photon microscopy studies⁵³ from $H_d = 0.1-0.9$ as shown in Figure 4(b).

Oxygen exchange

Vascular oxygen tension. Oxygen tension predictions in the blood vessels were compared to recent in vivo two-photon PO_2 microscopy mouse experiments⁵³ which measured arterial and venous RBC oxygen at different cortical depths. Figure 4(c) and Table 3 show that the predicted penetrating arteriole RBC oxygen content is fairly uniform between cortical layers, with an average of 69.2 ± 1.0 mmHg. The difference between the predicted arterial oxygen tension and measurements was less than 10%, which falls within the range of experimental error. The predicted venous RBC oxygen tension was

Table 3. Comparison of model predictions against experimental measurements.

Capillary Red Blood Cell Velocity 	mm/s 0.93±0.29 0.99±0.17 2.03±1.42 1.60±0.70 0.77±0.51 0.50±0.44 0.5-1.8 0.79±0.30 0.75±0.60	Reference This Work Charpak ⁵³ Unekawa ⁷⁵ Hudetz ⁷⁷ Kleinfeld ³⁴ Villringer ⁷⁸ Hudetz ² Ivanov ⁷⁹ Ma ⁸⁰
Cerebral Blood Perfusion^c 	mL/100g/min 78±16 ^b (19-101) 70-170 142±57 40-65	Reference This Work Xu ⁸¹ Maeda ⁸² Gertz ⁸³
Cerebral Oxygen Metabolism^c 	µmole/g/min 1.38±0.34 ^b (0.6-1.7) 1.31-2.96 1.5-3.2	Reference This Work Zhu ⁸⁴ Cui ⁵⁸
Penetrating Arteriole Vessel RBCs 	mmHg 69.2±1.0 68±17 65.6±1.69	Reference This Work Sakadzic ⁸⁵ Charpak ⁵³
Capillary RBCs 	38.4±4.0 43.3±2.0 36-56 66.3±1.6	Reference This Work Bailey ⁸⁶ Sakadzic ⁸⁵ Charpak ⁵³
Draining Venule Vessel RBCs 	35.8±3.0 ~35-48 39.4±0.7	Reference This Work Sakadzic ⁸⁵ Charpak ⁵³
Brain Tissue 	22.2±11.2 18-40 ^a 23	Reference This Work Erecinska ⁸⁷ Charpak ⁵³
Mitochondria 	21.9±11.1 ~20 14.6±4.1	Reference This Work Mik ⁸⁸ Bailey ⁸⁶

^aRat Measurement^bOmitting Data Set 2^cThe entire range of computed values from data set 1- 4 is indicated with a horizontal bar

between 34.2 and 41.3 mmHg. These results agree with the venous RBC oxygen tension of 39.4 ± 0.7 mmHg recently measured by the Charpak⁵³ lab.

Tissue oxygen tension. Figure 5 illustrates the simulated oxygen tension for the extravascular space. Figure 5(a)

shows that the tissue oxygen tension is everywhere lower than the arteriole and venule oxygen tension. The mean tissue oxygen tension was found to be 22.2 ± 11.2 mmHg, which is 45.1 mmHg lower than the mean arterial tension, 67.3 ± 3.6 mmHg, and 16.0 mmHg lower than the average venule, 38.2 ± 9.0 mmHg. Total oxygen

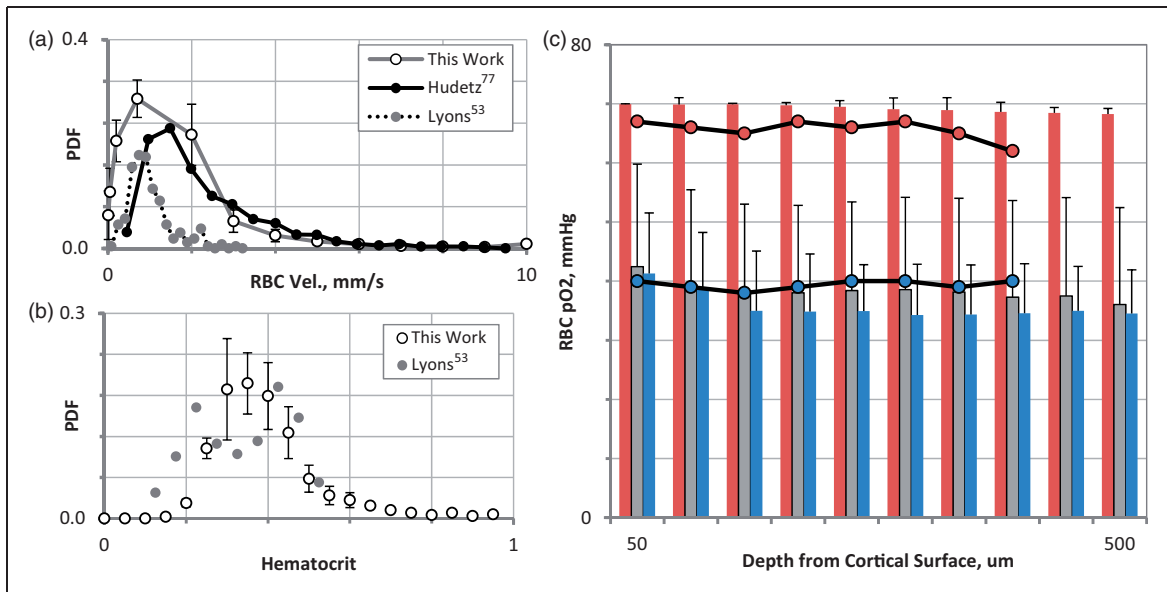


Figure 4. Comparison of predicted hematocrit distribution, RBC velocity, and RBC oxygen tension to measured data. (a) The predicted capillary RBC velocity matches measurements acquired with high-speed camera laser-scanning confocal microscopy.⁷⁵ Both simulation and experiment show that more than 88% of RBCs travel at speeds below 2 mm/s. (b) The PDF for capillary hematocrit shows that the majority of capillaries have a hematocrit between 0.25 and 0.50 comparing well to two-photon measurements.⁵³ (c) Mean RBC oxygen tension at different depths from the cortical surface (50-500 μm). Bars indicate arterial (red), capillary (gray), and venous (blue) RBC oxygen tension compared to measured data⁵³ drawn as lines with connected dots in red for arteries and veins in blue.

consumption in different compartments is summarized in Figure 5(b). Accordingly, tissues near arterioles (within a distance $< 10 \mu\text{m}$) were predicted to have higher oxygen metabolism, followed by tissues in the vicinity of venules. The average CMRO in the more distant tissues (distance $> 10 \mu\text{m}$) amounted to $1.15 \pm 0.93 \mu\text{mole/g/min}$.

Figure 5(c) to (f) reports characteristic oxygen concentration profiles in the tissue for all four data sets. The high resolution of extravascular oxygen tension was calculated using fine mesh discretization discussed in the Supplemental Information. Three-dimensional oxygen tension patterns in blood vessels are depicted in Figure 2(i). Here, tissue oxygen tension is plotted along three rays collinear with the x , y , and z axes penetrating the domain center as depicted in the inlay of Figure 5(c). Along all directions, the profiles show tissue oxygen tension spikes in the vicinity penetrating arterioles, whose locations are marked with red dotted lines. Oxygen tension is also elevated around draining venules marked with dotted blue lines. Between vessels, the tissue oxygen tension is relatively uniform with a mean of $22.2 \pm 11.2 \text{ mmHg}$. This fairly even oxygen tension falls within the physiological range of 18-40 mmHg, which is highlighted as a gray shaded box for clarity. Although the boundary zones follow similar trends, they are omitted in Figure 5 to limit the analysis to the core. Reported profiles were invariant to finer mesh resolutions with edge lengths of $6.6 \mu\text{m}$, thus demonstrating mesh independence (see Supplemental Information).

Prediction of intracellular oxygen gradients

Subcellular oxygen tensions in the ECS, neuronal cytoplasm, and neuronal mitochondria were predicted using the vectorized neuronal and glial data in combination with the spatial distribution procedure illustrated in Figure 6(a) for the glial mitochondria and Figure 6(b) for neuronal mitochondria. For cortical layers I-IV oxygen tension differences between the ECS, neuronal cytoplasm and neuronal mitochondria are displayed in Figure 6(c). The schematic in Figure 6(d) illustrates the differences between the ECS, neuronal cell cytoplasm (N), glial cell cytoplasm (G) and mitochondrial oxygen tension. The mean oxygen tension in the cytoplasm of the neurons in the four layers is $25.90 \pm 11.15 \text{ mmHg}$, slightly lower than the oxygen tension in the ECS ($25.91 \pm 11.16 \text{ mmHg}$). The oxygen gradient across the neuronal cell membrane was $134 \times 10^{-6} \text{ mmHg}$. The oxygen tension in the neuronal cytoplasm was $250 \times 10^{-6} \text{ mmHg}$ above the mitochondria as shown in Figure 6(c). Intracellular oxygen tension was simultaneously predicted for glial cells. The oxygen tension in the glial cytoplasm is $25.90 \pm 11.16 \text{ mmHg}$, which is $134 \times 10^{-6} \text{ mmHg}$ below the surrounding ECS. It should be noted that both kinetic models of oxygen consumption yield comparable oxygen metabolism rates. However, only the mitochondrial model allows predicting oxygen gradients between the ECS, the cytoplasm, and the mitochondria. The

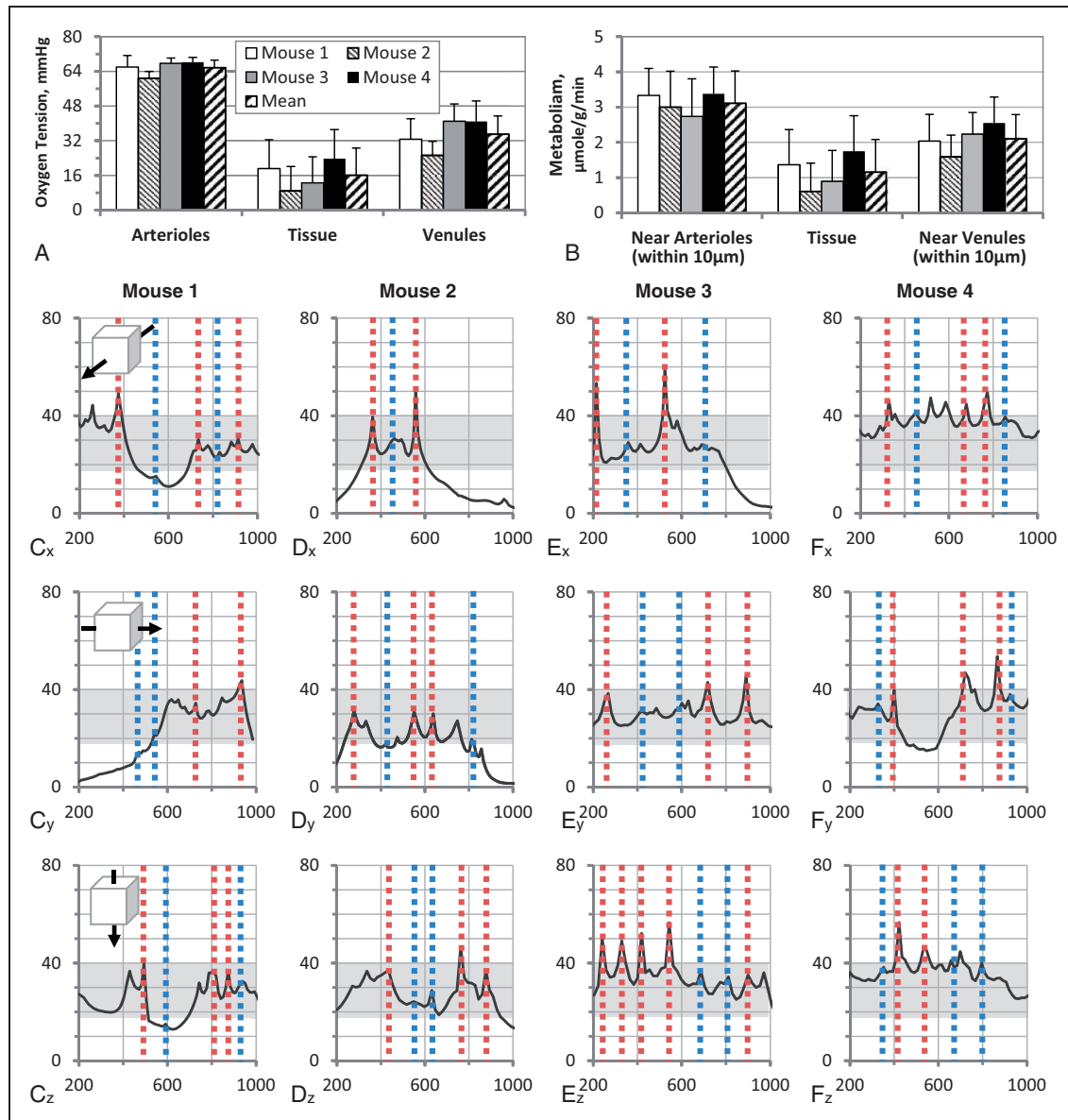


Figure 5. Oxygen tension in the murine cortical tissue. (a) Average oxygen tension in the arterioles, tissue, and venules in all four data sets, standard deviation as capped lines. The tissue is an oxygen sink and therefore lower than both arteries and veins. (b) Oxygen metabolism as a function of proximity to penetrating vessel. Oxygen tension along a ray passing through the center of each of the four data sets (c-f) in the x-direction, y-direction, and z-direction. Dotted vertical lines illustrate the position of penetrating arterioles (red) and penetrating venules (blue), gray box indicates experimentally measured oxygen tension in the murine cortex (18–40 mmHg).

first-order oxygen metabolism model does not resolve individual intracellular oxygen differences because the three compartments are lumped.

Path analysis

To better understand spatial variations of hemodynamic states, path analysis from all arterial inlets to venous outlets was performed. Blood pressure, hematocrit, RBC saturation, and plasma oxygen tension

trajectories along several representative paths for mouse one were analyzed and plotted as a function of diameter in Figure 7. Each path begins at an arterial inlet and follows the direction of blood flow, making random choices at each bifurcation, thus traversing the capillary bed and returning to the surface through a draining pial vein. All possible paths were enumerated and the maximum and minimum values are painted as shaded regions in Figure 7(b) to (f). The average trajectory of each hemodynamic state was plotted as a black solid line.

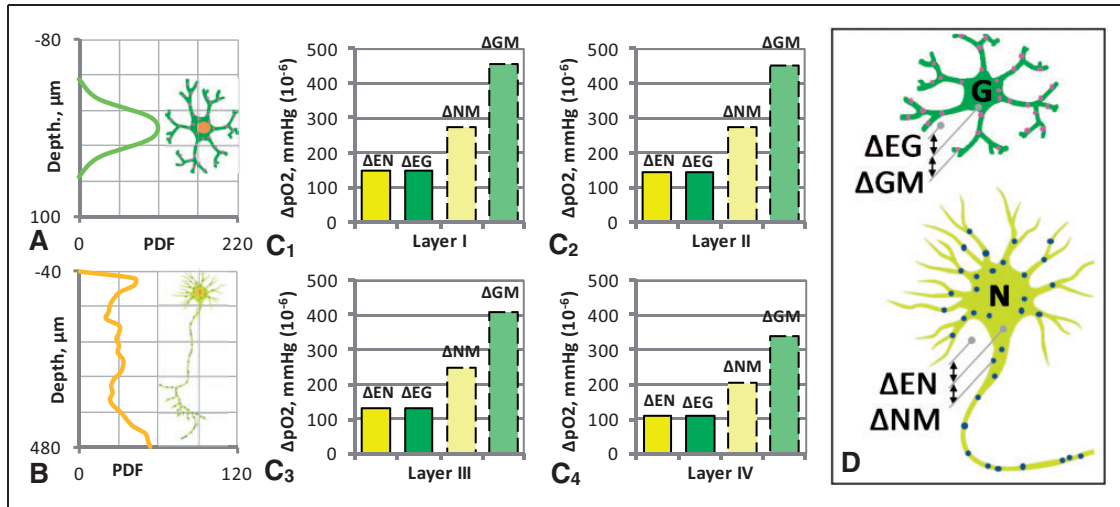


Figure 6. Predicted tissue, cellular, and intercellular oxygen gradients. Mitochondria were spatially distributed to different location with the respect to the cell nucleus according to a cell-specific PDF: (a) PDF for mitochondria location around glial nucleus ($x=0$ mm) (b) PDF of mitochondria in neurons. C_1 - C_4 . Oxygen tension gradient between ECS and neuronal cytoplasm (ΔEN), neuronal cytoplasm and mitochondria (ΔNM), ECS and glial cell cytoplasm (ΔEG), and glial cell cytoplasm to glial mitochondria (ΔGM) are reported for cortical layers I-IV. (d) Illustration of the differences between the ECS, neuronal cell cytoplasm (N), glial cell cytoplasm (G), and mitochondrial oxygen tension.

The pressure was recorded for all paths for each of the four data sets, and the average pressure drop is shown in Figure 7(b). Minimum and maximum pressures along all paths (data not shown) are depicted as a shaded region. Blood pressure decreases monotonically in each path displayed in Figure 7(c), which is consistent with the flow direction of the blood supply. The pressure drop is steepest in capillaries ($d < 10 \mu\text{m}$) including small vessels fed by adjacent penetrating arterioles. The locations of these steep pressure drops suggest that the capillary bed is the major site of blood flow resistance.

In addition, five representative paths were traced individually in the first data set and are drawn as solid lines of different colors as illustrated in Figure 7(a). The hemodynamic states of blood pressure, hematocrit, RBC saturation, and plasma oxygen tension were taken along each of these paths. Hematocrit tends to concentrate in deep reaching penetrating arterioles due to *plasma skimming* as shown in Figure 7(d). For example, in some paths (green path), the hematocrit of penetrating arterioles rises to $H_d=0.60$ which is higher than its pial supply vessel of $H_d=0.35$. Paths connecting to the capillary bed closer to the surface (orange path), tend to have lower hematocrit than paths traveling deeper into the cortex. The RBC content in the capillary bed is highly variable depending on the location and hematocrit of its feeders. Some segments are more concentrated, $H_d=0.60$, or more dilute, $H_d=0.11$, than the systemic hematocrit. In venules, the highly variable red blood cell concentration in the capillaries is remixed.

Therefore, the discharge hematocrit in draining veins returns to $H_d=0.35$.

The RBC oxygen saturation remains fairly constant at 83% in the thick-walled surface arteries and penetrating arterioles as depicted in Figure 7(e). Oxygen saturation then drops dramatically where the penetrating arterioles feed the thin-walled capillary bed. Depending on the path, RBC saturation decreased anywhere to 10% (purple and blue path) to very low values (green and orange path) in the capillary bed. This variability in oxygen saturation in the capillary bed depends on the path length and orientation. All paths eventually feed into the draining venules, from highly concentrated (58%, blue path) to low saturation (45%, orange path). This variability in RBC saturation is reflected in the plasma oxygen tension depicted in Figure 7(f).

Discussion

The complex interaction of microcirculatory network topology, oxygen metabolism, and hemodynamics was quantified by detailed simulations reaching down to the cellular level. Microvessels were labeled by size, cortical depth, and hierarchy. Non-Newtonian biphasic hemodynamics, RBC velocity, RBC saturation, and oxygen turnover were predicted throughout the primary somatosensory cortex of four animals. Intracellular oxygen gradients between the cytoplasm and mitochondrial oxygen tension inside neurons and glial cells were also computed. Through the interrogation of every path

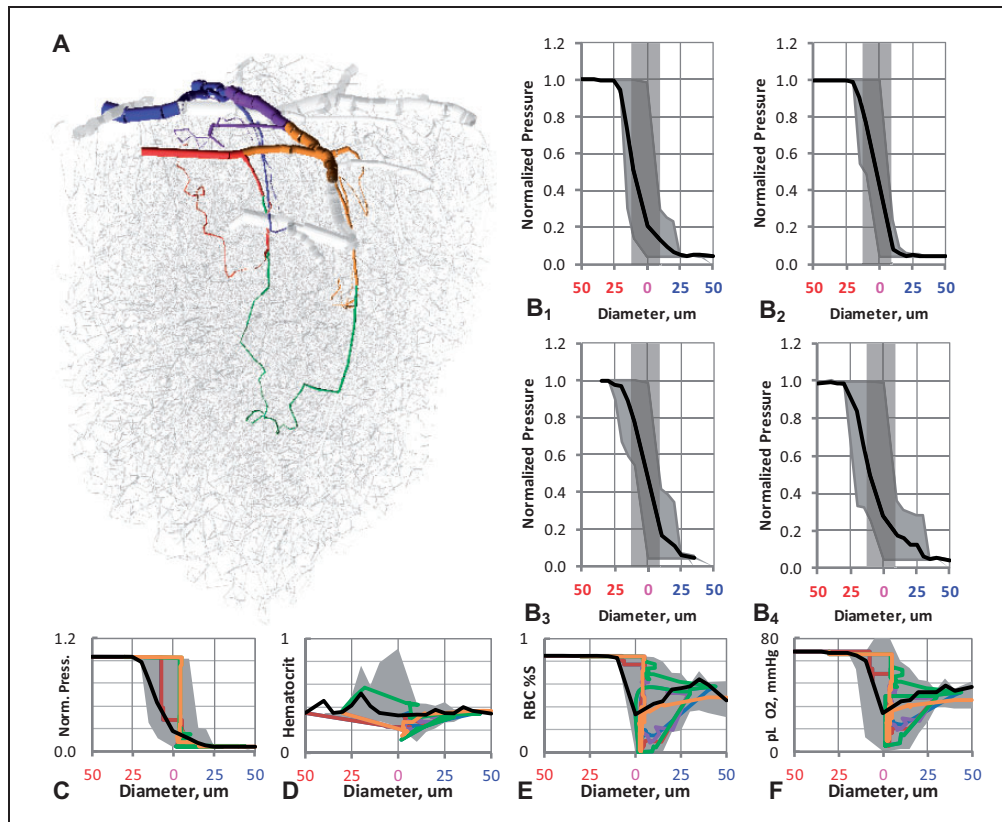


Figure 7. Path analysis in a representative data set (mouse one). (a) Anatomy of the cortical microcirculation with five typical flow paths. Each path follows the blood flow from an inlet pial artery through the capillary bed returning to the surface via draining venules. B₁–B₄. Mean pressure paths and range of microcirculatory blood pressure shown for all four data sets. Light gray shaded box indicates the capillary bed (vessels with diameter < 10 μm), where the main pressure drop occurs. This shaded region includes pre-capillary arterioles, capillaries, and post-capillary venules. (c–f) The computed hemodynamic trajectory of each flow path is reported for (c) blood pressure, (d) discharge hematocrit, (e) RBC saturation, and (f) plasma pO_2 . Upper and lower ranges of all paths (only five individual paths are shown) are drawn as a gray shaded region, illustrating the heterogeneity of the capillary bed. Averages of all paths are drawn as a black line. Note that averages do not well characterize the wide variety of hemodynamic state transitions that occur in the capillary bed.

through the cortical blood supply, a quantitative picture of all *hemodynamic state transitions* inside the microcirculation emerges. The computational results identify capillaries adjacent to feeding arterioles and the capillary bed ($d < 10 \mu\text{m}$) as the major site of hemodynamic resistance.

Hemodynamics and variability along microcirculatory paths

Simulations show that even capillaries with identical blood flow, caliber, and path length may convey RBCs at different velocities. Though capillary diameter and path length contribute to blood flow resistance, the variability of RBC velocity within the capillary bed depends on hematocrit fluctuations. Plasma skimming concentrates RBCs in deeper reaching penetrating arterioles, while paths near the surface tend to be

more dilute. Concentration of RBCs in the penetrating arterioles ensures that deep tissue near the gray-white matter interface is well-supplied with oxygen and nutrients. The KPSM was chosen over prior models because it can compute RBC splitting at trifurcations and higher order vessel junctions. Table 3 offers a comprehensive comparison of all predications against known experimental results. It shows that our model agrees reasonably with most known experimental values at the macroscopical blood flow level as well as subcellular properties such as mitochondrial oxygen tension.

Like hematocrit, RBC oxygen tension varies little in the surface pial arteries. Below the cortical surface in the microcirculation, the random arrangement of the blood vessels creates a multiplicity of paths producing a wide spectrum of blood pressures, hematocrit, and RBC tensions. The path analysis further shows that blood pressures, hematocrit, and oxygen tension

cannot be attributed to blood vessels by diameter or membership within an ordered hierarchy. Moreover, there is no “standard” trajectory of hemodynamic state transitions; this finding has important implications for experiments.

Individual experimental point measurements only describe a single path, which in general do not coincide with other paths in the same cortical section or those acquired in a different animal. Discrepancies reported in the literature may not indicate experimental error, but merely reflect the wide variability of the natural hemodynamic states in the microcirculation. In order to confirm our predictions of the variance in the capillary bed, numerous measurements in three dimensional tissue samples instead of point measurements are needed.

Microcirculatory resistance distribution

The path analysis reported in Figure 7(b) clearly indicated that the largest pressure drops occur in the smallest vessels ($d < 10 \mu\text{m}$). Accordingly, it appears that these small vessels contribute the bulk of the hemodynamic resistance. While this model does not differentiate between pre-capillary arterioles or post-arteriole capillaries, it is clear that the majority of hydraulic resistance lies near and around the capillary bed, and not in the penetrating arterioles. Tracing individual paths through the microcirculation, as indicated by the colored lines in Figure 7(c), show that the steepest pressure drops occur in the capillary bed.

Limitations

The comparison to experimental data shows that cerebral blood perfusion as well as cerebral oxygen metabolism is at the lower end of the experimental trends indicating a reduced inflow of blood and oxygen. We believe that some microvessels may not have been recognized by the image reconstruction software so that the current model, although anatomically fairly complete, may still miss vessels present in the real cortex. These issues were partially compensated by our choice to use a relatively high inlet pressure.

The criterion for differentiating between small arterioles and capillaries relied on branching order and vessel diameter; *actin* and *desmin* labeling of the parent data set to differentiate between pre-capillary arterioles and post-arteriole capillaries is not available at this time. The original data sets contained arteriolar loops that did not connect to the capillary bed. These non-physiologic “dead-end loops” were corrected by connecting them to the capillary bed to ensure flow through every vessel. None of the four cortical samples had

more than 30 dead-end-loops, which is equivalent to less than 0.1% of all blood vessel segments – a minimal change to the original data.

Not all smooth muscle and endothelial cells were detected; therefore, the metabolic demands of these cell types could not be incorporated in this study which may underestimate oxygen extraction by muscle cells in the wall of larger arterial vessels. Furthermore, because the position of mitochondria was not determined, a spatial distribution of mitochondria inside the neurons and glial cells was assumed according to a probabilistic density function. Extracellular and mitochondrial oxygen tensions between simulations and experiments matched well, but cytoplasmic oxygen tension is experimentally inaccessible at this time. Because glucose transport, carboxylic acid production, and pH calculation were not addressed in this work, oxygen binding kinetics were computed using a set $\text{pH} = 7.4$. A pH sensitive computation of oxygen binding kinetics using the Adair et al.⁸⁹ model may be an appropriate step forward. A more complex model⁹⁰ of oxygen and glucose metabolism could also shed insight into the controlling factors for CMRO.

Future work

The predicted wide range of hemodynamic values in the capillary bed underscores the difficulty in comparing point measurements between different experiments, animal specimens, laboratories, or computer simulations. This work suggests that the variation of blood pressure, flow, and oxygen tension may be wider than previously expected. Recent experimental studies of oxygen distribution in the cerebral microcirculation^{53,85} confirm the patchiness of hemodynamic states within the capillary bed. Accordingly, multiple measurements tracing numerous paths from the surface pials down to the capillary bed are needed for meaningful characterization of microcirculatory flow patterns and validation.

The capillary bed, specifically capillaries adjacent to feeding arterioles, was identified as the primary site of flow resistance. While dilation of a single capillary hardly changes global blood flow, a concerted dilation of capillaries in a sizeable cortical subsection would drastically reduce the hemodynamic resistance thus increasing blood perfusion to that region. Accordingly, adjustments of capillary bed resistance may serve to regulate tissue perfusion in response to brain injury. On the other hand, the smooth muscles of arteries and arterioles enable control over blood supply from the cortical surface to the deep layers. This second potentially fast activation of the arterial blood supply via vasodilation and constriction may be activated during functional hyperemia. Detailed models of cerebral microcirculation such as the system presented here may in the future aide

in determining the role of vasoconstriction of arterioles or pericytes in regulating cortical blood perfusion.

Funding

The authors disclosed receipt of the following financial support for the research, authorship, and/or publication of this article: The authors would like to acknowledge the National Science Foundation for partial support through EAGER Grant No. CBET-1301198 (L. Achenie, M. Burka, NSF Program Directors). DK additionally acknowledges the National Institutes of Health awards DP1 NS082097 and R01 EB003832.

Declaration of conflicting interests

The author(s) declared no potential conflicts of interest with respect to the research, authorship, and/or publication of this article.

Authors' contributions

Two-photon microscopy images, data filtering, and construction of the microcirculation topology for all four data sets were performed by DK and PT at University of California San Diego. Computational simulations, figure design, and text are credited to AL and IG at University of Illinois Chicago. Both groups contributed to the technical content of this manuscript.

Supplementary material

Supplementary material for this paper can be found at <http://jcbfm.sagepub.com/content/by/supplemental-data>

References

- Devor A, Sakadzic S, Saisan PA, et al. "Overshoot" of O₂ is required to maintain baseline tissue oxygenation at locations distal to blood vessels. *J Neurosci* 2011; 31: 13676–13681.
- Hudetz AG. Blood flow in the cerebral capillary network: a review emphasizing observations with intravital microscopy. *Microcirculation* 1997; 4: 233–252.
- Boas DA, Jones SR, Devor A, et al. A vascular anatomical network model of the spatio-temporal response to brain activation. *Neuroimage* 2008; 40: 1116–1129.
- Kaufmann AM, Firlik AD, Fukui MB, et al. Ischemic core and penumbra in human stroke. *Stroke* 1999; 30: 93–99.
- Nishimura N, Schaffer CB, Friedman B, et al. Penetrating arterioles are a bottleneck in the perfusion of neocortex. *Proc Natl Acad Sci U S A* 2007; 104: 365–370.
- Gertz K, Priller J, Kronenberg G, et al. Physical activity improves long-term stroke outcome via endothelial nitric oxide synthase-dependent augmentation of neovascularization and cerebral blood flow. *Circ Res* 2006; 99: 1132–1140.
- Shih AY, Friedman B, Drew PJ, et al. Active dilation of penetrating arterioles restores red blood cell flux to penumbral neocortex after focal stroke. *J Cereb Blood Flow Metab* 2009; 29: 738–751.
- Helmchen F and Kleinfeld D. In vivo measurements of blood flow and glial cell function with two-photon laser-scanning microscopy. *Angiogenesis* 2008; 444(Pt A): 231–254.
- del Zoppo GJ and Mabuchi T. Cerebral microvessel responses to focal ischemia. *J Cereb Blood Flow Metab* 2003; 23: 879–894.
- Reglin B and Pries AR. Metabolic control of microvascular networks: oxygen sensing and beyond. *J Vasc Res* 2014; 51: 376–392.
- Lecoq J, Parpaleix A, Roussakis E, et al. Simultaneous two-photon imaging of oxygen and blood flow in deep cerebral vessels. *Nat Med* 2011; 17: 893–898.
- Zonta M, Angulo MC, Gobbo S, et al. Neuron-to-astrocyte signaling is central to the dynamic control of brain microcirculation. *Nat Neurosci* 2003; 6: 43–50.
- Pittman RN. Oxygen transport in the microcirculation and its regulation. *Microcirculation* 2013; 20: 117–137.
- Goldman D and Popel AS. Computational modeling of oxygen transport from complex capillary networks. Relation to the microcirculation physiome. *Adv Exp Med Biol* 1999; 471: 555–563.
- Tsoukias NM, Goldman D, Vadapalli A, et al. A computational model of oxygen delivery by hemoglobin-based oxygen carriers in three-dimensional microvascular networks. *J Theor Biol* 2007; 248: 657–674.
- Secomb TW and Pries AR. Blood viscosity in microvessels: experiment and theory. *Comptes Rendus Physique* 2013; 14: 470–478.
- Gould IG and Linninger AA. Hematocrit distribution and tissue oxygenation in large microcirculatory networks. *Microcirculation* 2015; 22: 1–18.
- Duvernoy H, Delon S and Vannson JL. The vascularization of the cerebellar cortex. *Brain Res Bull* 1983; 11: 419–480.
- Cassot F, Lauwers F, Lorthois S, et al. Branching patterns for arterioles and venules of the human cerebral cortex. *Brain Res* 2010; 1313: 62–78.
- Duvernoy HM, Delon S and Vannson JL. Cortical blood vessels of the human brain. *Brain Res Bull* 1981; 7: 519–579.
- Lauwers F, Cassot F, Lauwers-Cances V, et al. Morphometry of the human cerebral cortex microcirculation: general characteristics and space-related profiles. *Neuroimage* 2008; 39: 936–948.
- Intaglietta M, Johnson PC and Winslow RM. Microvascular and tissue oxygen distribution. *Cardiovasc Res* 1996; 32: 632–643.
- Vovenko EP and Chuikin AE. Tissue oxygen tension profiles close to brain arterioles and venules in the rat cerebral cortex during the development of acute anemia. *Neurosci Behav Physiol* 2010; 40: 723–731.
- Vovenko EP and Chuikin AE. Oxygen tension in rat cerebral cortex microvessels in acute anemia. *Neurosci Behav Physiol* 2008; 38: 493–500.
- Krogh A. The supply of oxygen to the tissues and the regulation of the capillary circulation. *J Physiol* 1919; 52: 457–474.
- Kirkpatrick JP and Dewhirst MW. Analytic solution to steady-state radial diffusion of a substrate with first-order

- reaction kinetics in the tissue of a Krogh's cylinder. *Radiat Res* 2008; 169: 350–354.
27. Huppert TJ, Allen MS, Benav H, et al. A multicompart-ment vascular model for inferring baseline and functional changes in cerebral oxygen metabolism and arterial dilation. *J Cereb Blood Flow Metab* 2007; 27: 1262–1279.
 28. Smith AF, Secomb TW, Pries AR, et al. Structure-based algorithms for microvessel classification. *Microcirculation* 2015; 22: 99–108.
 29. Fang Q, Sakadzic S, Ruvinskaya L, et al. Oxygen advec-tion and diffusion in a three- dimensional vascular ana-tomical network. *Opt Express* 2008; 16: 17530–17541.
 30. Hellums JD, Nair PK, Huang NS, et al. Simulation of intraluminal gas transport processes in the microcircula-tion. *Ann Biomed Eng* 1996; 24: 1–24.
 31. Goldman D. Theoretical models of microvascular oxygen transport to tissue. *Microcirculation* 2008; 15: 795–811.
 32. Zweifach BW and Lipowsky HH. Quantitative studies of microcirculatory structure and function. III. Microvascular hemodynamics of cat mesentery and rabbit omentum. *Circ Res* 1977; 41: 380–390.
 33. Pries AR, Ley K and Gaetgens P. Generalization of the fahraeus principle for microvessel networks. *Am J Physiol* 1986; 251: H1324–H1332.
 34. Kleinfeld D, Mitra PP, Helmchen F, et al. Fluctuations and stimulus-induced changes in blood flow observed in individual capillaries in layers 2 through 4 of rat neocor-tex. *Proc Natl Acad Sci U S A* 1998; 95: 15741–15746.
 35. Safaeian N and David T. A computational model of oxygen transport in the cerebrocapillary levels for normal and pathologic brain function. *J Cereb Blood Flow Metab* 2013; 33: 1633–1641.
 36. Schneider M, Hirsch S, Weber B, et al. Physiologically based construction of optimized 3-D arterial tree models. *Med Image Comput Comput Assist Interv* 2011; 14: 404–411.
 37. Goldman D and Popel AS. A computational study of the effect of capillary network anastomoses and tortuosity on oxygen transport. *J Theor Biol* 2000; 206: 181–194.
 38. Lorthois S, Cassot F and Lauwers F. Simulation study of brain blood flow regulation by intra-cortical arterioles in an anatomically accurate large human vascular network: Part I: methodology and baseline flow. *Neuroimage* 2011; 54: 1031–1042.
 39. Linninger AA, Gould IG, Marinnan T, et al. Cerebral microcirculation and oxygen tension in the human sec-ondary cortex. *Ann Biomed Eng* 2013; 41: 2264–2284.
 40. Karch R, Neumann F, Neumann M, et al. Staged growth of optimized arterial model trees. *Ann Biomed Eng* 2000; 28: 495–511.
 41. Blinder P, Tsai PS, Kaufhold JP, et al. The cortical angio-me: an interconnected vascular network with non-columnar patterns of blood flow. *Nat Neurosci* 2013; 16: 889–897.
 42. Tsai PS, Kaufhold JP, Blinder P, et al. Correlations of neuronal and microvascular densities in murine cortex revealed by direct counting and colocalization of nuclei and vessels. *J Neurosci* 2009; 29: 14553–14570.
 43. Kaufhold JP, Tsai PS, Blinder P, et al. Vectorization of optically sectioned brain microvasculature: learning aids completion of vascular graphs by connecting gaps and deleting open-ended segments. *Med Image Anal* 2012; 16: 1241–1258.
 44. Shih AY, Driscoll JD, Drew PJ, et al. Two-photon microscopy as a tool to study blood flow and neurovas-cular coupling in the rodent brain. *J Cereb Blood Flow Metab* 2012; 32: 1277–1309.
 45. Zhang K and Sejnowski TJ. A universal scaling law between gray matter and white matter of cerebral cortex. *Proc Natl Acad Sci U S A* 2000; 97: 5621–5626.
 46. Hall CN, Reynell C, Gesslein B, et al. Capillary pericytes regulate cerebral blood flow in health and disease. *Nature* 2014; 508: 55–60.
 47. Hill RA, Tong L, Yuan P, et al. Regional blood flow in the normal and ischemic brain is controlled by arteriolar smooth muscle cell contractility and not by capillary peri-cytes. *Neuron* 2015; 87: 95–110.
 48. Shih AY, Rühlmann C, Blinder P, et al. Robust and fragile aspects of cortical blood flow in relation to the underlying angioarchitecture. *Microcirculation* 2015; 22: 204–218.
 49. Fahraeus R. The suspension stability of the blood. *Physiol Rev* 1929; 9: 241–274.
 50. Pries AR and Secomb TW. Microvascular blood viscosity in vivo and the endothelial surface layer. *Am J Physiol Heart Circ Physiol* 2005; 289: H2657–H2664.
 51. Morimoto S, Cassell MD, Beltz TG, et al. Elevated blood pressure in transgenic mice with brain-specific expression of human angiotensinogen driven by the glial fibrillary acidic protein promoter. *Circ Res* 2001; 89: 365–372.
 52. Oshio K, Watanabe H, Song Y, et al. Reduced cerebrospinal fluid production and intracranial pressure in mice lacking choroid plexus water channel Aquaporin-1. *FASEB J* 2005; 19: 76–78.
 53. Lyons D, Parpaleix A, Roche M, et al. Mapping oxygen concentration in the awake mouse brain. *eLife* 2016; 5: e12024.
 54. Liu G, Mac Gabhann F and Popel AS. Effects of fiber type and size on the heterogeneity of oxygen distribution in exercising skeletal muscle. *PLoS One* 2012; 7: e44375.
 55. Christoforides C, Laasberg LH and Hedley-Whyte J. Effect of temperature on solubility of O₂ in human plasma. *J Appl Physiol* 1969; 26: 56–60.
 56. Mintun MA, Lundstrom BN, Snyder AZ, et al. Blood flow and oxygen delivery to human brain during func-tional activity: theoretical modeling and experimental data. *Proc Natl Acad Sci U S A* 2001; 98: 6859–6864.
 57. Ellis CG, Bateman RM, Sharpe MD, et al. Effect of a maldistribution of microvascular blood flow on capillary O₂ extraction in sepsis. *Am J Physiol Heart Circ Physiol* 2002; 282: H156–H164.
 58. Cui WN, Zhu XH, Vollmers ML, et al. Non-invasive measurement of cerebral oxygen metabolism in the mouse brain by ultra-high field O-17 MR spectroscopy. *J Cereb Blood Flow Metab* 2013; 33: 1846–1849.
 59. Rodriguez JJ, Yeh CY, Terzieva S, et al. Complex and region-specific changes in astroglial markers in the aging brain. *Neurobiol Aging* 2014; 35: 15–23.
 60. Hoppeler H, Hudlicka O and Uhlmann E. Relationship between mitochondria and oxygen-consumption in iso-lated cat muscles. *J Physiol* 1987; 385: 661–675.

61. Howard CV, Jolleys G, Stacey D, et al. Measurement of total neuronal volume, surface area, and dendritic length following intracellular physiological recording. *Neuroprotocols* 1993; 2: 113–120.
62. Popel AS, Pittman RN and Ellsworth ML. Rate of oxygen loss from arterioles is an order of magnitude higher than expected. *Am J Physiol* 1989; 256: H921–H924.
63. Schmitt FO. Fibrous proteins-neuronal organelles. *Proc Natl Acad Sci U S A* 1968; 60: 1092–1011.
64. Sjostrand FS and Cassell RZ. Structure of inner membranes in rat heart muscle mitochondria as revealed by means of freeze-fracturing. *J Ultrastruct Res* 1978; 63: 111–137.
65. Williams V, Grossman RG and Edmunds SM. Volume and surface area estimates of astrocytes in the sensorimotor cortex of the cat. *Neuroscience* 1980; 5: 1151–1159.
66. Hill AV. The combinations of haemoglobin with oxygen and with carbon monoxide. I. *Biochem J* 1913; 7: 471–480.
67. Hill AV. The combinations of haemoglobin with oxygen and carbon monoxide, and the effects of acid and carbon dioxide. *Biochem J* 1921; 15: 577–586.
68. Miller KE and Sheetz MP. Axonal mitochondrial transport and potential are correlated. *J Cell Sci* 2004; 117: 2791–2804.
69. Nafstad PH and Blackstad TW. Distribution of mitochondria in pyramidal cells and boutons in hippocampal cortex. *Z Zellforsch Mikrosk Anat* 1966; 73: 234–245.
70. Holash JA, Noden DM and Stewart PA. Re-evaluating the role of astrocytes in blood-brain barrier induction. *Dev Dyn* 1993; 197: 14–25.
71. Schnitzer J. Immunocytochemical studies on the development of astrocytes, Muller (glial) cells, and oligodendrocytes in the rabbit retina. *Brain Res Dev Brain Res* 1988; 44: 59–72.
72. Jou MJ, Peng TI and Sheu SS. Histamine induces oscillations of mitochondrial free Ca²⁺ concentration in single cultured rat brain astrocytes. *J Physiol* 1996; 497(Pt 2): 299–308.
73. Trans-NIH Knock-Out Mouse Project (KOMP) U01HG004080-04S1 supplemental Recovery Act funds: KOMP Repository at UC Davis and CHORI (U42RR024244).
74. Reichold J, Stampanoni M, Lena Keller A, et al. Vascular graph model to simulate the cerebral blood flow in realistic vascular networks. *J Cereb Blood Flow Metab* 2009; 29: 1429–1443.
75. Uekawa M, Tomita M, Tomita Y, et al. RBC velocities in single capillaries of mouse and rat brains are the same, despite 10-fold difference in body size. *Brain Res* 2010; 1320: 69–73.
76. Errico C, Pierre J, Pezet S, et al. Ultrafast ultrasound localization microscopy for deep super-resolution vascular imaging. *Nature* 2015; 527: 499–502.
77. Hudetz AG, Feher G and Kampine JP. Heterogeneous autoregulation of cerebrocortical capillary flow: evidence for functional thoroughfare channels? *Microvasc Res* 1996; 51: 131–136.
78. Villringer A, Them A, Lindauer U, et al. Capillary perfusion of the rat brain cortex. An in vivo confocal microscopy study. *Circ Res* 1994; 75: 55–62.
79. Ivanov KP, Kalinina MK and Levkovich Yu I. Blood flow velocity in capillaries of brain and muscles and its physiological significance. *Microvasc Res* 1981; 22: 143–155.
80. Ma YP, Koo A, Kwan HC, et al. On-line measurement of the dynamic velocity of erythrocytes in the cerebral microvessels in the rat. *Microvasc Res* 1974; 8: 1–13.
81. Xu K, Radhakrishnan K, Serhal A, et al. In: JC LaManna (ed.) *Oxygen transport to tissue XXXII*, Springer Science+Business Media, 2011.
82. Maeda K, Mies G, Olah L, et al. Quantitative measurement of local cerebral blood flow in the anesthetized mouse using intraperitoneal [C-14]iodoantipyrine injection and final arterial heart blood sampling. *J Cereb Blood Flow Metab* 2000; 20: 10–14.
83. Gertz K, Priller J, Kronenberg G, et al. Physical activity improves long-term stroke outcome via endothelial nitric oxide synthase-dependent augmentation of neovascularization and cerebral blood flow. *Circ Res* 2006; 99: 1132–1140.
84. Zhu XH, Zhang Y, Tian RX, et al. Development of O-17 NMR approach for fast imaging of cerebral metabolic rate of oxygen in rat brain at high field. *Proc Natl Acad Sci U S A* 2002; 99: 13194–13199.
85. Sakadzic S, Mandeville ET, Gagnon L, et al. Large arteriolar component of oxygen delivery implies a safe margin of oxygen supply to cerebral tissue. *Nat Commun* 2014; 5: 5734.
86. Bailey DM, Taudorf S, Berg RMG, et al. Cerebral formation of free radicals during hypoxia does not cause structural damage and is associated with a reduction in mitochondrial PO₂; evidence of O-2-sensing in humans? *J Cereb Blood Flow Metab* 2011; 31: 1020–1026.
87. Erecinska M and Silver IA. Tissue oxygen tension and brain sensitivity to hypoxia. *Resp Physiol* 2001; 128: 263–276.
88. Mik EG, Johannes T, Zuurbier CJ, et al. In vivo mitochondrial oxygen tension measured by a delayed fluorescence lifetime technique. *Biophys J* 2008; 95: 3977–3990.
89. Adair GS, Bock AV and Field HJ. The hemoglobin system: VI. The oxygen dissociation curve of hemoglobin. *J Biol Chem* 1925; 63: 529–545.
90. Kembro JM, Aon MA, Winslow RL, et al. Integrating mitochondrial energetics, redox and ROS metabolic networks: a two-compartment model. *Biophys J* 2013; 104: 657a–a.